Environmental Science and Pollution Research (2023) 30:3027–3044
https://doi.org/10.1007/s11356-022-22402-4

RESEARCH ARTICLE

Effective removal of cationic dye on activated carbon made from cactus fruit peels: a combined experimental and theoretical study

Imane Akkari[1] · Zahra Graba[1] · Nacer Bezzi[1] · Mohamed Mehdi Kaci[2] · Farid Ait Merzeg[1,3] · Nadia Bait[3] · Azedine Ferhati[4] · Guilherme L. Dotto[5] · Yacine Benguerba[6]

Received: 18 May 2022 / Accepted: 1 August 2022 / Published online: 8 August 2022

Abstract

This article investigates experimentally and theoretically the adsorption of Basic Red 46 cationic dye (BR46) using activated carbon generated from cactus fruit peels (ACCFP). The prepared adsorbent was characterized by different analytical tools showing a good surface for the uptake of pollutants. A maximum batch adsorption capacity of 806.38 mg g^{-1} was achieved at optimal conditions. The Freundlich model best represented the equilibrium data, although the pseudo-second-order kinetic model best described the adsorption kinetics. The thermodynamic studies demonstrated that the adsorption process was spontaneous ($\Delta G° < 0$) and endothermic ($\Delta H° = 32.512$ kJ mol^{-1}). DFT descriptors were combined with COSMO-RS and AIM theory to provide a complete picture of the adsorbate/adsorbent system and its molecular interactions. Last, the ACCFP was regenerable up to four times, emphasizing the idea of using it as an adsorbent to treat textile wastewaters.

Keywords Activated carbon · Adsorption · Basic Red 46 · Cactus fruit peels · DFT, AIM, COSMO-RS models

Introduction

Environmental protection from industrial waste has become an urgent concern due to industrialization (Kaci et al. 2021b). Heavy metals and aromatic dyes are only some harmful substances found in industrial discharges (Kaci et al. 2021a). Cationic dyes are widely employed and dispersed in the aquatic environment due to their inhibitory properties (Atmani et al. 2022). The human health effects of its emission into effluents are substantial (cancer, mutations, skin irritation, and allergic dermatitis). Because of its inability to decompose, it reduces the photosynthetic activity of aquatic organisms. Our planet requires quick action to safeguard the ecosystem from pollution sources, particularly the introduction of low-concentration poisons into the water (Lemaoui et al. 2020d; Hammoudi et al. 2021; Hammoudi et al. 2022).

Textile and leather dyes are available in various formulations, including Basic Red 46, and cationic dyes represent a significant risk to marine life and the surrounding environment (Wong et al. 2018). Numerous chemical (Kaci et al. 2022), physical (Akkari et al. 2022), and biological (Paz et al. 2017) techniques for removing these persistent pollutants are being evaluated (Toumi et al. 2019). Adsorption is emerging as a viable option for industrial

---

Responsible Editor: Philippe Garrigues

✉ Yacine Benguerba
yacinebenguerba@univ-setif.dz

[1] Materials Technology and Process Engineering Laboratory (LTMGP), University of Bejaia, 06000 Bejaia, Algeria

[2] Laboratory of Reaction Engineering, Faculty of Mechanical and Process Engineering (USTHB), BP 32, 16111 Algiers, Algeria

[3] Research Unit on Analyses and Technological Development in Environment (UR-ADTE)/Scientific and Technical Research Centre in Physical and Chemical Analyses (CRAPC), BP 384, Zone Industrielle, RP, 42004 Bou-Ismail, Tipaza, Algeria

[4] Laboratory of Chemistry and Environmental Chemistry (LCCE), University of Batna 1, Batna, Algeria

[5] Research Group on Adsorptive and Catalytic Process Engineering (ENGEPAC), Federal University of Santa Maria, Av. Roraima, 1000-7, Santa Maria, RS 97105–900, Brazil

[6] Laboratoire de Biopharmacie Et Pharmacotechnie (LBPT), Ferhat Abbas Setif 1 University, Setif, Algeria

effluent dye removal because of its simplicity of design, safety, efficacy, ease of operation, adaptability, environmental friendliness, and cheap cost (Xiao et al. 2020).

Basic Red 46 is widely used in the textile industry, accounting for about 10% of global dye output, and is classified as a hazardous organic chemical (Şentürk and Yıldız 2020). Due to their inability to adhere to fibers, considerable amounts of color are liberated into the effluent. Additionally, they are not physiologically biodegradable due to their aromatic character. Recently, numerous adsorbents' adsorption capacities for the elimination of Basic Red 46 were disclosed, with the nature and synthesis process having a significant effect on adsorption capacities. Activated carbon derived from Ziziphus lotus stones has an adsorption capacity of 307 mg g^{-1} (Boudechiche et al. 2019). Similarly, Kaouah et al. (2013) obtained a 781.25 mg g^{-1}. Şentürk and Yıldız (2020) determined that activated pine sawdust contained 312.5 mg g^{-1}. On the other hand, Konicki et al. (2018) reported obtaining 46.7 mg g^{-1} of Fe@graphite core-shell by chemical vapor deposition, whereas 370.4 mg g^{-1} was reported utilizing graphene oxide (Shoushtarian et al. 2020).

Activated carbon (AC) is the most widely utilized adsorbent because of its vast surface area, porous porosity, and high reactivity (Novais et al. 2018). However, commercial activated carbons may be excessively expensive and are often manufactured from nonrenewable sources like coal and waste products from the petroleum industry (Jawad et al. 2020). Therefore, numerous research has used biowaste to synthesize activated carbons as a low-cost and renewable starting material (Vieira et al. 2021). Agricultural by-products have been widely researched as lignocellulosic precursors in recent years, with promising results as they have the potential to create valuable materials such as adsorbents, electrodes, and catalysts (Baysal et al. 2018; Elmouwahidi et al. 2018). (Mateo et al. 2020). Additionally, several ACs have been successfully synthesized using fruit peels, including orange peels (Souza et al. 2018), dragon fruit peels (Jawad et al. 2021), apple peels (Enniya et al. 2018), banana peels (Prastuti et al. 2019), and mongo peels (Mukherjee et al. 2019).

The method by which AC is produced significantly influences its qualities. Chemical and physical activation are the most prevalent forms. On the other hand, chemical activation exhibited several benefits, including lower activation temperatures, improved yields, and well-developed porosity (Kumar and Jena 2017; Ruiz et al. 2017). Hence, activation agents such as H_3PO_4, $ZnCl_2$, and alkaline metal complexes have been explored in this field. Additional advantages of H_3PO_4 include improved AC generation with non-hazardous qualities and the absence of the requirement for anything other than water purification (Francoeur et al. 2021).

Cactus fruit, Cactaceae, is distributed around the world in semi-arid conditions. It is widespread over Latin America, Africa, and the Mediterranean (Saenz 2000). Although it is well known for its nutritional benefits, it has lately attracted more medicinal attention (Shetty et al. 2012; Berraaouan et al. 2015). However, its peels and seeds are often discarded as low-cost solid waste during industrial operations. These agricultural "waste" products are high in bioactive chemicals and dietary fiber. Most peels are composed of cellulose, pectin, lignin, and gums. Despite this, only a few studies have shown the production of adsorbents from cactus fruit peels. Insufficient literature is readily available: Kumar and Barakat (2013) used cactus fruit peels to remove the fruit's vibrant green color; Mohamed et al. (2020) utilized thermally treated cactus pear peels to adsorb methylene blue, and Gebrezgiher and Kiflie (2020) used HCl-pretreated cactus fruit peels to adsorb reactive colors. Unfortunately, no thermochemical activation of cactus fruit peels with H_3PO_4 has been documented to produce activated carbon for color removal applications.

This study focused on synthesizing activated carbon utilizing cactus fruit peels as a precursor, characterized by various techniques for removing Basic Red 46 from aqueous media. The operational parameters governing the adsorption process are optimized, and the isotherm, kinetic, thermodynamic, and regeneration characteristics are discussed. In addition, DFT global reactivity descriptors, COSMO-RS, and AIM investigations were employed to better understand the BR46 adsorption mechanism on ACCFP in aqueous solutions.

Experimental part

Preparation of dye solution

Basic Red 46 (BR46) was provided by a local textile company and utilized (Fig. 1). As a first step, the powder was dissolved in distilled water to make a 1 g L^{-1} reserve solution. It was then diluted to the appropriate concentrations for the test solutions. A pH meter (BOECO BT-675) and HCl (0.1M) or NaOH (0.1M) were used to adjust the pH.

Preparation of activated carbon

Cactus fruit peels were washed and dried for 24 h at 80 °C before being crushed and screen-selected to a 500-µm size. Two grams of this precursor was combined with a phosphoric acid solution at room temperature with a 4:1 H_3PO_4/precursor ratio. The mixture was dried for 2 h at 100 °C in an oven. The sample was then heated to 600 °C for an hour with an N_2 flow (70 mL min^{-1}). The preparation conditions of this material are based on previous studies on different biomass (Abatan et al. 2019; Tang and Ahmad Zaini 2020). After activation, it was cooled to room temperature, rinsed with hot distilled water to

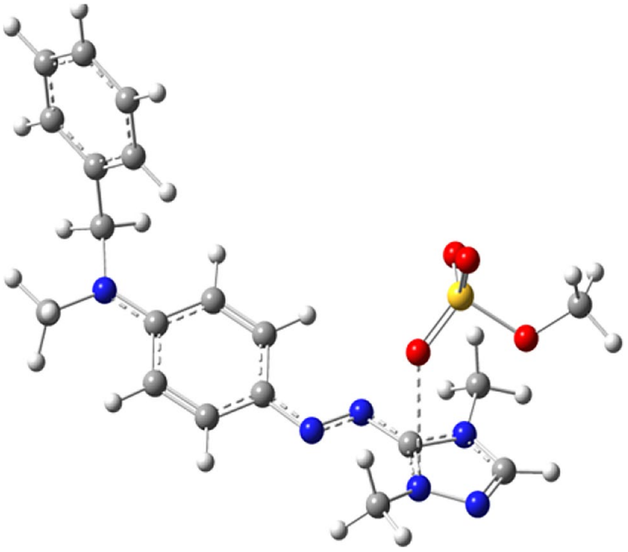

Fig. 1 Three-dimensional and planar molecular structure of Basic Red 46

neutralize the pH, crushed, and sieved to a particle size of 100 µm. Dehydrators were used to keep the ACCFP dry.

Characterization

By employing X-ray diffractometers equipped with CuKα radiation sources (λ = 1.5418 Å) in the 10–80° range, the crystallized phase was identified. A scanning electron microscope (SEM; Quanta 650) with an EDS device was used to examine the microstructure and elemental composition of the sample. The XPS measures were taken using a Kratos axis supra spectrometer, which had constant pass energy of 20 eV, and a dual X-ray source consisting of Al K (1486.6 eV). The surface chemical groups were investigated using Fourier transform infrared spectroscopy (FTIR) using a Nicolet IS5 Spectrophotometer in the range 500–4000 cm^{-1} (resolution 0.4 cm^{-1}; a scan rate 40 scans min^{-1}). A Micromeritics ASAP 2010 device measured the specific surface area (SBET) for N_2 adsorption at low temperatures. Pore size distributions were calculated using the Barrett–Joyner–Halenda (BJH) model. Several Erlenmeyer flasks were filled with 50 mL of 0.01 M NaCl solution to identify the point of zero charges (pH_{pzc}). HCl and NaOH solutions were used to modify the pH of each solution to the desired levels. ACCFP (0.15 g per Erlenmeyer flask) was then added. The pH of the mixture was measured after it had been vigorously agitated for 24 h. The pH_{pzc} is the point on the bisector where the curve between pH_{final} and $pH_{initial}$ crosses. The Boehm titration method measured the ACCFP's surface functional groups (Boehm 2002). Agitation for 48 h with the addition of 0.5 g ACCFP resulted in 50 mL solutions of 0.01 N $NaHCO_3$, Na_2CO_3, NaOH, and HCl. Titrations with NaOH or HCl (0.01 N) were performed. The number of acidic surface groups was calculated using the assumptions that NaOH neutralizes lactonic phenolic and carboxylic groups, Na_2CO_3 neutralizes lactonic and carboxylic groups, and $NaHCO_3$ neutralizes just carboxylic groups. At the same time, the amount of HCl interacted with ACCFP to identify the alkaline surface locations.

Experiments on adsorption

Tests were performed with the 1-L conical flask sample using 500 mL dye solutions, and the starting concentration of 200 mg L^{-1} was held for 120 min for the BR46 adsorbent. Reuse and kinetic thermodynamic studies were carried out under optimum operating conditions. After equilibration, the samples were centrifuged at 6000 rpm for 10 min. A UV-visible spectrophotometer (SHIMADZU UV-1800) was used to measure the absorbance of several dye solutions at (λ_{max} = 531 nm) to estimate the concentration of BR46.

The following equations were used to compute the adsorption capacity (q) and removal rate (R):

$$q_{(e,t)} = \frac{\left(C_0 - C_{(e,t)}\right) V}{M} \tag{1}$$

$$R_{(e,t)} = \frac{\left(C_0 - C_{(e,t)}\right)}{C_0} \times 100 \tag{2}$$

The starting dye concentration is C_o (mg L^{-1}), the equilibrium and time dye concentrations are C_e and C_t (mg L^{-1}), the volume of dye solution is V (L), and M (g) is the adsorbent dosage.

Computational study

The Turbomole software was used to perform the computational investigations (Aissaoui et al. 2017). The geometry of three molecular structures (BR46, ACCFP, and BR@ACCFP) was optimized using the generalized gradient approximation GGA-BP86 functional with the TZVP basis (Lemaoui et al. 2020c, b; Almustafa et al. 2021; Darwish et al. 2021). Convergence was required to occur with a maximum energy change of 10^{-6} Ha and a gradient change of 10^{-3} Ha/Bohr (Lemaoui et al. 2020a, 2021).

The electrical parameters of the three molecules were calculated, including the chemical potential (μ), global hardness (η), electrophilicity index (ω), and ΔN, which reflects the fraction of electrons transferred from BR46 to the ACCFP surface (Benabid et al. 2019a).

$$\mu = -\chi = \left(E_{\text{HOMO}} + E_{\text{LUMO}}\right)/2 \tag{3}$$

$$\eta = \left(-E_{\mathrm{HOMO}} + E_{\mathrm{LUMO}}\right)/2 \tag{4}$$

$$\omega = \mu^2/2\eta \tag{5}$$

$$\Delta N = \frac{\chi_{\mathrm{BR46}} - \chi_{\mathrm{ACCFP}}}{2\left(\eta_{\mathrm{BR46}} + \eta_{\mathrm{ACCFP}}\right)} \tag{6}$$

E_{HOMO} and E_{LUMO} denote HOMO and LUMO orbitals' energy; χ denotes electronegativity (Benabid et al. 2021; Bououden et al. 2021).

The adsorption energy of the investigated system was calculated using the following equation:

$$E_{\mathrm{ads}} = E_{\mathrm{BR46@ACCFP}} - \left(E_{\mathrm{BR46}} + E_{\mathrm{ACCFP}}\right) \tag{7}$$

$E_{\mathrm{BR46@ACCFP}}$ denotes the optimized structure energy of the adsorbed BR46 on ACCFP; E_{BR46} and E_{ACCFP} denote the optimized structure energies of the isolated BR46 and ACCFP molecules.

The solubilization process of the molecule was studied using COSMO-RS.

AIM's primary purpose is to study the type and intensity of bonding interactions in molecular systems using molecules' electron density $\rho(r)$. The second derivative $\nabla 2\rho(r)$ sign may be used to identify the kind of chemical bonds present at the binding critical point (BCP) (Shainyan et al. 2010; Kurnia et al. 2015). The covalent (polar) connection is shown if the value is large and the $\nabla^2\rho(r)$ is negative (Grabowski and Ugalde 2010). System rivalry between electron grouping (potential energy), $V(r)$, and diffusion through electronic mobility (kinetic energy), $G(r)$, are shown by the $|V|/G$ ratio. An excess of electric charges creates the interaction when the ratio $|V|/G > 1$.

Interactions are classified as:

- Pure interactions with closed layers, $|V|/G < 1$.
- Interactions with closed layers, $1 < |V|/G < 2$.
- Interactions with shared layer, $|V|/G > 2$.

Hydrogen bonding is classified under the first two types, whereas covalent interactions are classified under the third. Positive $\nabla^2\rho(r)$ and $H(r) = V(r) + G(r)$ values indicate electrostatic interaction, and negative values indicate a covalent connection. A partially covalent bond has a positive $\nabla^2\rho(r)$ and a negative $H(r)$ value (Rozas et al. 2000).

The amsterdam density functional (ADF) was employed in AIM calculations (Chen et al. 2020; Bououden et al. 2021). The molecular structure was optimized using the DFT-B3LYP functional at a TZVP basis (Te Velde et al. 2001; Bououden et al. 2021).

Results and discussion

Characterization of activated carbon

XRD analysis was used to verify the prepared activated carbon's amorphous characteristics (Fig. 2). The crystal faces (002) and (100) in the typical diffraction patterns of activated carbon's amorphous phase (JCPDS 00-001-0646) are remarkably consistent with the two values at 24° and 44.6° (Ma and Ouyang 2013; Koyuncu et al. 2018).

SEM was utilized to characterize the microstructure of ACCFP (Fig. 3). for ACCFP samples before (Fig. 3a, b) and after dye adsorption (Fig. 3b, d). The ACCFP (Fig. 3a, b) demonstrated irregular particle morphologies with a rough heterogeneous surface with cavities ranging from 5.25 to 8.64 µm. After adsorption, Fig. 3c, d show that the ACCFP surface became smoother as the cavities decreased up to 1.65 µm, as well as the accumulation of ACCFP particles, which may indicate that the dye molecules have been trapped and uptaken on the adsorbent surface.

The elemental composition of ACCFP was determined before and after adsorption using EDS microanalysis (Fig. 3e, f). As shown in Fig. 3e, this activated carbon has a high carbon content (70.34%), as well as the presence of additional elements such as O (16.31%) and P (9.5%), as well as trace levels of Ca (3%) and K (0.65%). Even though the carbon content (79.43%) after adsorption increased due to color molecules, which suggests that BR46 was adsorbed successfully onto the surface (Table 1).

XPS analysis was exploited to identify and measure the elemental and chemical states of the surface of ACCFP (Fig. 4). According to the survey scan (Fig. 4a), ACCFP is mainly composed of carbon C (40%), oxygen O (44.3%), and phosphorus P (13.3%), with negligible quantities of calcium Ca (2.3%) and nitrogen N (0.1%). The C 1s spectrum (Fig. 4b) is deconvoluted into three peaks, located at 283.8, 284.56, and 286.99 eV that are ascribed to the aliphatic/aromatic group (C–C/C–H), the hydroxyl group (C–O), and carbonyl group (C=O), respectively (Wu et al. 2021b; Xiong et al. 2021). Furthermore, the O 1s spectrum (Fig. 4c) may be split into three distinct peaks, at 530.96, 532.47, and 532.80 eV, attributed to C=O, C–O, and C–OH, respectively (Jang et al. 2018; Wu et al. 2021a).

FTIR spectra may be utilized to determine the chemical structure and functional groups of ACCFP before and during adsorption with BR46 (Fig. 5). Before adsorption, the band at 3700 cm^{-1} is produced by overlapping hydroxyl and amine groups (OH and NH) (Mokhtar et al. 2017). The bands at 3080 and 2950 cm^{-1} are attributed to the methyl and methylene groups C=H elongation

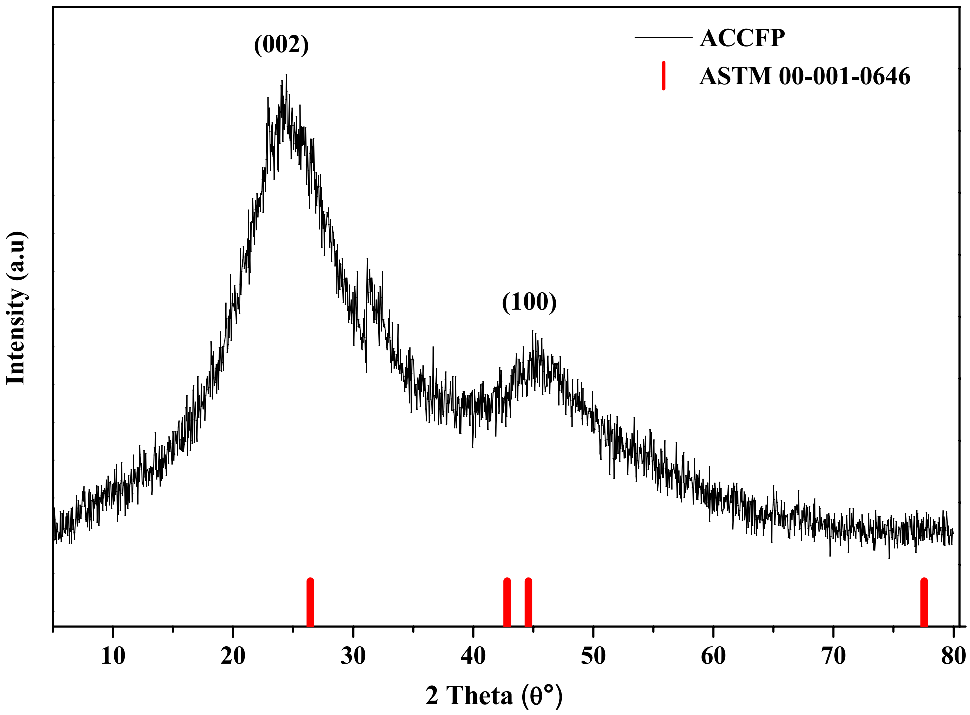

Fig. 2 XRD spectrum of the obtained ACCFP powder

vibrations (Niazi et al. 2018). At 1790 cm^{-1}, the C=O band of the carbonyl group may be found (Xue et al. 2022). The band at 1570 cm^{-1} may be ascribed to CH deformation-induced vibrations. The peak at 1250 cm^{-1} might be due to CN stretching in amino acids (Yu and Luo 2014). The peak at 1090 cm^{-1} could result from the POC stretching vibration, while the peak at 786 cm^{-1} could result from the PO band (Bagheri et al. 2020). At 918 cm^{-1}, the peak is consistent with NH deformation. Following adsorption, the ACCFP spectrum reveals a slight change in the location of almost all peaks, showing that distinct functional groups of ACCFP are involved in the absorption of BR46.

The surface-specific area of ACCFP was measured before and after adsorption utilizing the BET adsorption-desorption of N_2. The nitrogen adsorption/desorption isotherms for ACCFP before and after dye adsorption are shown in Fig. 6a, b, together with an inset displaying the dye's associated Barrett–Joyner–Halenda (BJH) pore size distribution.

According to the IUPAC classification, ACCFP features a typical V-IV hybrid isotherm curve completely overlapped and devoid of a hysteresis loop, indicating microporous (Kumar and Jena 2017). Additionally, as shown in Table 2, the specific surface area of ACCFP was 1288 and 432.6 $m^2\ g^{-1}$ before and after adsorption. In contrast, the pore size is generally less than 10 nm, showing that ACCFP has a microporous structure. Accordingly, the decrease in the specific surface area and the pore volume of the ACCFP sample after dye adsorption may be due to the occupation of the pores by the dye molecules. Moreover, it may be due to the agglomeration of the adsorbent particles after adsorption.

The zero charge is included in the pH characteristic of the accumulated electric charge on the surface (pH_{pzc}), represented by the point of intersection of the pH_{final} vs. $pH_{initial}$ curves with the bisector. ACCFP surfaces are positively charged with pH less than 2.05 and negatively charged for more than 2.05 (Fig. 7). At $pH > pH_{pzc}$, the ACCFP surface functional groups deprotonate, resulting in a negative charge (Momčilović et al. 2012).

The Boehm titration results are given in Table 3. The pH_{pzc} and Boehm titration results indicate that ACCFP exhibits an acidic behavior resulting from the H_3PO_4 modification (Liu et al. 2010).

Adsorption measurements

The adsorption experiments were conducted in triplicate, and the average standard deviation was around 0.45%.

Solution pH effect

The adsorbent's surface charge and the electrostatic interactions between the adsorbent and the adsorbed molecules are directly influenced by the adsorbent's initial pH (Goswami and Phukan 2017). The effect of pH was investigated in the range of 2 to 10. Adsorption capacity was 137.44 mg g^{-1} ($R = 68.72\%$) at pH = 2, rising to 180.70 mg g^{-1} ($R = 90.35\%$) at pH = 6, and then progressively decreasing (Fig. 8a). A reduction in adsorption capacity occurs when the pH dips

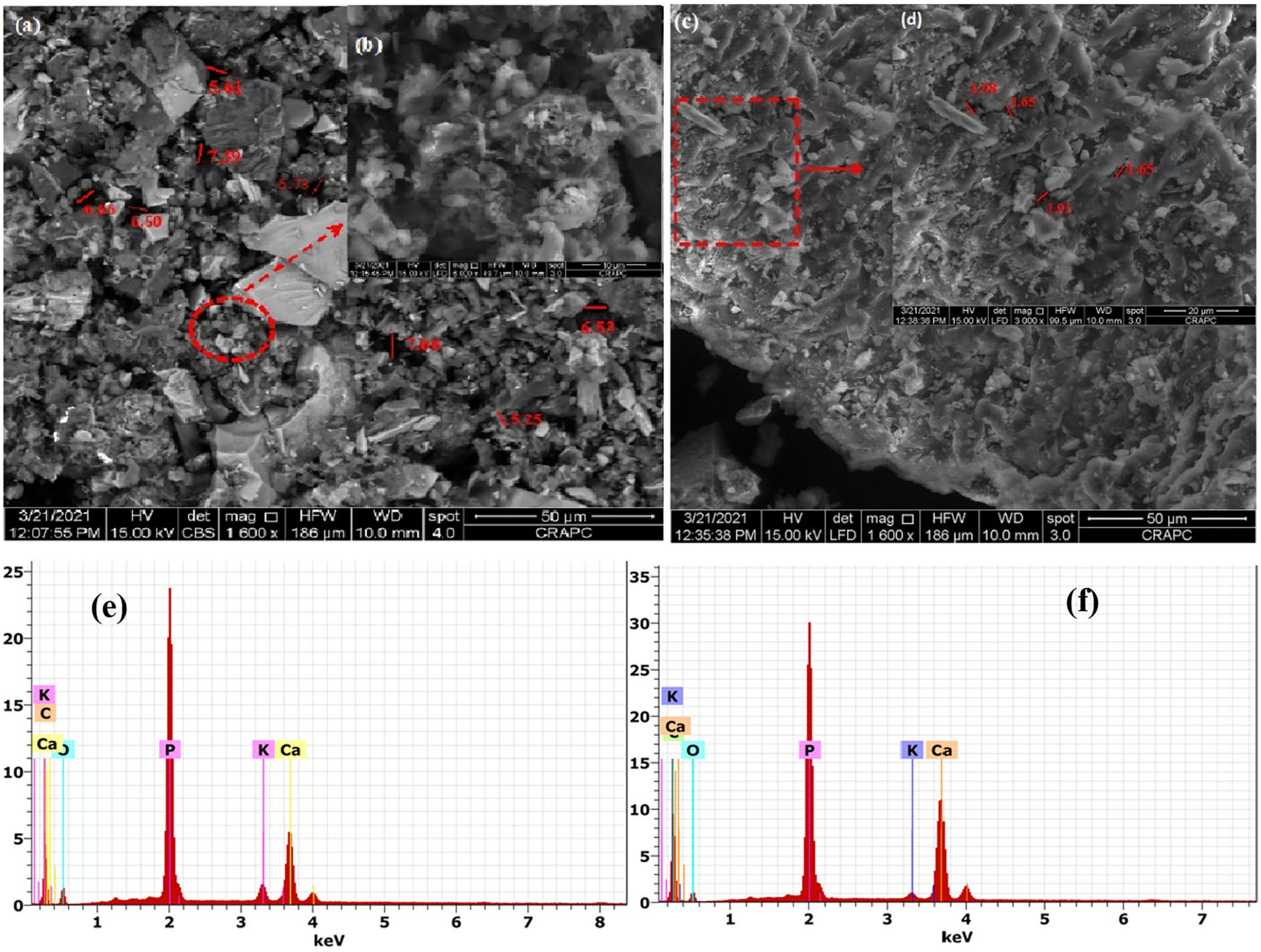

Fig. 3 Characterization of the ACCFP sample by SEM (before (**a**, **b**) and after (**c**, **d**) adsorption) and EDS (before (**e**) and after (**f**) adsorption)

Table 1 ACCFP elemental composition

Element	Before adsorption (%)	After adsorption (%)
Carbon C	70.34	79.43
Oxygen O	16.31	9.99
Phosphorus P	9.71	7.70
Calcium	3	2.66
Potassium	0.65	0.22

below $pH_{pzc} = 2.05$, owing to repulsive forces and competition between the H_3O^+ and the dye's cation for the adsorption sites. The favorable electrostatic interactions between the anionic surface of the adsorbent and the cation of the dye molecule led to the improvement of cation adsorption when pH is higher than pH_{pzc} (Kuppusamy et al. 2017; Xiong et al. 2021). Hydroxyl anions surrounding BR46 may be responsible for reducing retention at higher pH levels.

ACCFP dose effect

There was an investigation of adsorbent dosages displayed in Fig. 8a. The adsorption capacity fell from 515.10 mg g^{-1} ($R = 51.51\%$) to 47.26 mg g^{-1} (94.53%) when the adsorbent concentration was raised from 0.2 to 4 g L^{-1}. In other cases, adsorption capacity decreases because particular adsorption sites have been unsaturated. However, a more significant surface area and more adsorption sites at higher adsorbent doses may also increase removal (Rengaraj et al. 2004; Mohanty et al. 2005). A negligible increase in the removal rate was observed for adsorbent doses greater than or equal to 1 g L^{-1}, which is why this dose was retained for the rest of the sorption tests.

Stirring speed effect

Figure 8c shows a study examining the impact of stirring speed, ranging from 100 to 700 rpm. To begin, the absorption capacity at 100 rpm was 174.73 mg g^{-1} ($R = 87.63\%$),

Fig. 4 XPS spectra: ACCFP (**a**), carbon (**b**), and oxygen (**c**)

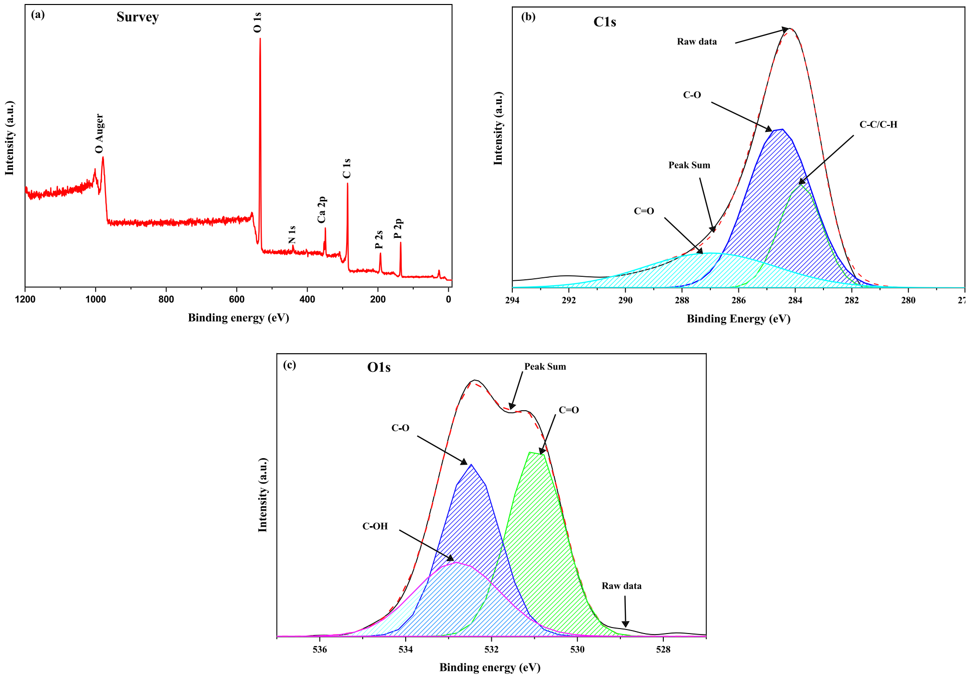

Fig. 5 FTIR spectra of ACCFP

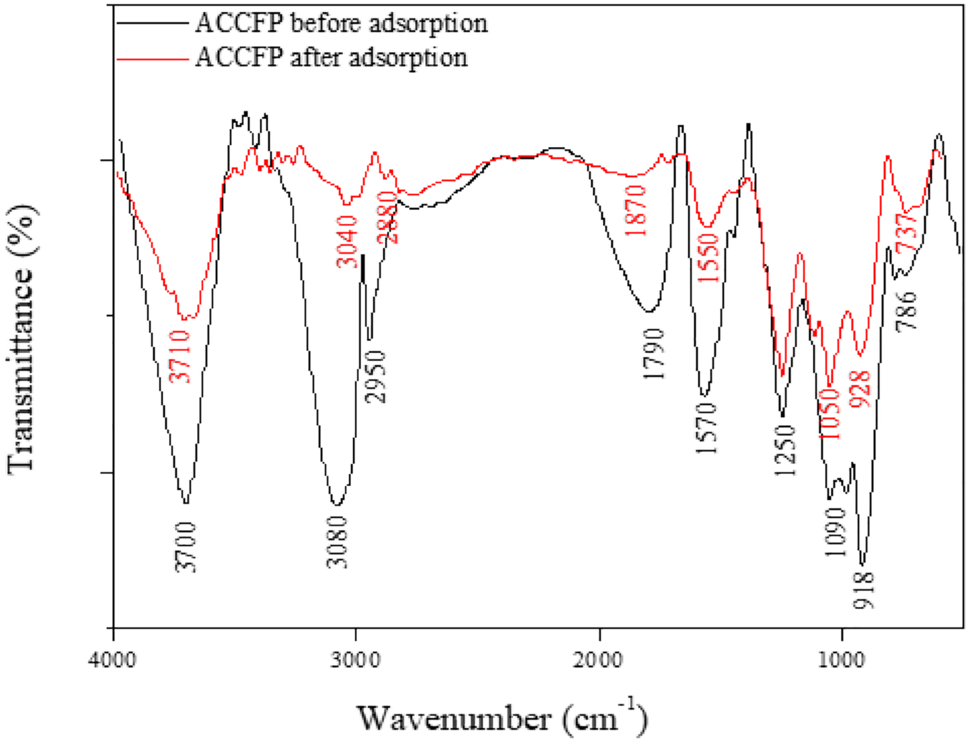

rising to 180.70 mg g^{-1} ($R = 90.35\%$) at 500 rpm. After that, the adsorption capacity decreased. Stirring speed facilitates dye solution dispersion within the adsorbent particles by reducing mass transfer resistance (Zhao et al. 2013). Increasing the speed reduces the adsorption capacity because a portion of the adsorbent is balanced against flask walls.

Temperature effect

Figure 8d depicts the effect of temperature on the adsorption of BR46 onto ACCFP. At temperatures ranging from 25 to 50 °C, the adsorption of BR46 by ACCFP is endothermic, as demonstrated by an increase in adsorption capacity from 180

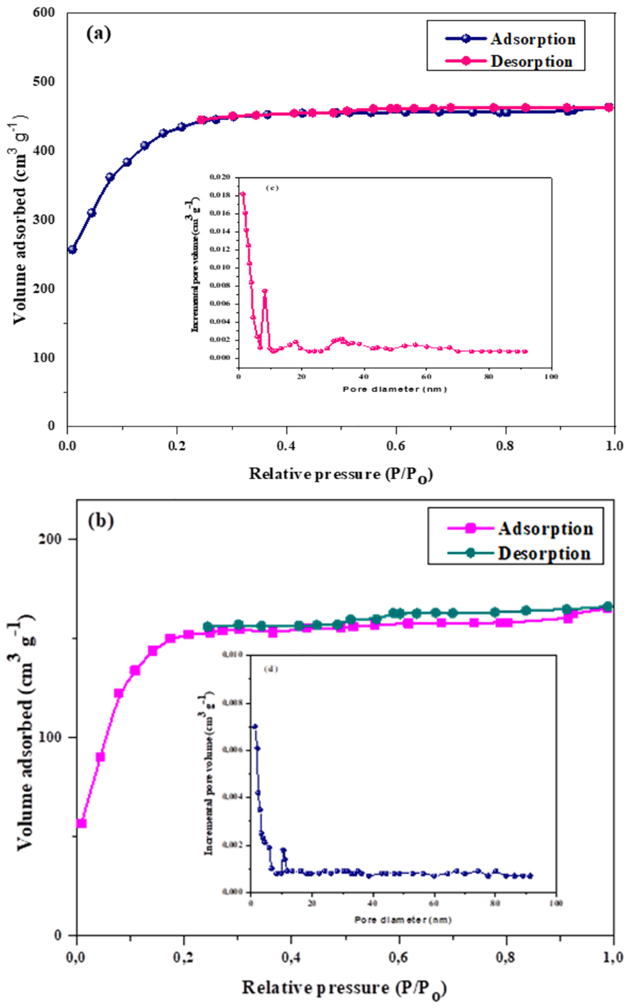

Fig. 6 N_2 isotherms (**a**, **b**). BJH pore size distribution of ACCFP (**c, d**)

Table 2 Textural features of ACCFP

	Specific surface area (m² g^{-1})	Pore volume (cm^3 g^{-1})	Pore size (nm)
Before adsorption	1288	0.744	1.940
After adsorption	432.6	0.098	0.421

mg g^{-1} ($R = 90.35\%$) to 193.85 mg g^{-1} (96.92%) (Hameed and Ahmad 2009; Arora et al. 2019).

Time and BR46 initial concentration effects

Figure 8e illustrates the effect of altering the initial BR46 concentrations (i.e., 20, 50, 100, 200, 500, and 1000 mg g^{-1}) at various time intervals (0–180 min). Due to a lack of adsorption sites, equilibrium was not reached until after 180 min, whereas it was rapid during the first 30 min. Hence, the mass transfer increase may be due to an increase in adsorption capacity from 19.74 mg g^{-1} ($R = 98.71\%$) to 806.38 mg g^{-1} ($R = 80.63\%$) (Naushad et al. 2019).

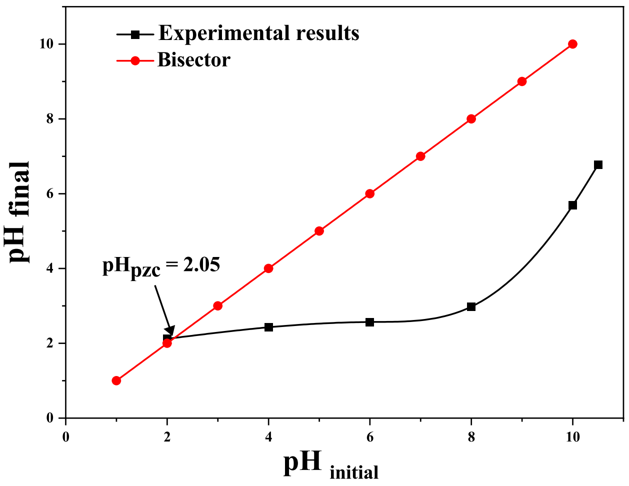

Fig. 7 pH_{pzc} of ACCFP

Table 3 Boehm titration of ACCFP

Parameter	Value
Carboxylic groups (mmol g^{-1})	1.09
Lactonic groups (mmol g^{-1})	0.57
Phenolic grous (mmol g^{-1})	0.03
Total Surface acidity (mmol g^{-1})	1.69
Total Surface basicity (mmol g^{-1})	0.68

Adsorption modeling

Adsorption isotherms

Four isotherm models were examined to fully comprehend the interactions between dye molecules and the adsorbent surface (Langmuir, Freundlich, Temkin, and Dubinin-Radushkevich). Under optimum circumstances (pH = 6, 25 °C, 500 rpm, 180-min contact duration, and 1 g L^{-1} of adsorbent), equilibrium experiments were carried out with dye concentrations of 20, 50, 100, 200, 500, and 1000 mg L^{-1}.

The Langmuir model (Langmuir 1918) proposes that monolayer adsorption may occur on a homogenous surface (Benabid et al. 2019b). According to the Freundlich model (Freundlich 1906), adsorption takes place on a heterogeneous surface, which includes interactions between molecules that have been adsorbed. Temkin's model considers interactions between the adsorbent and the adsorbed molecules during the adsorption process

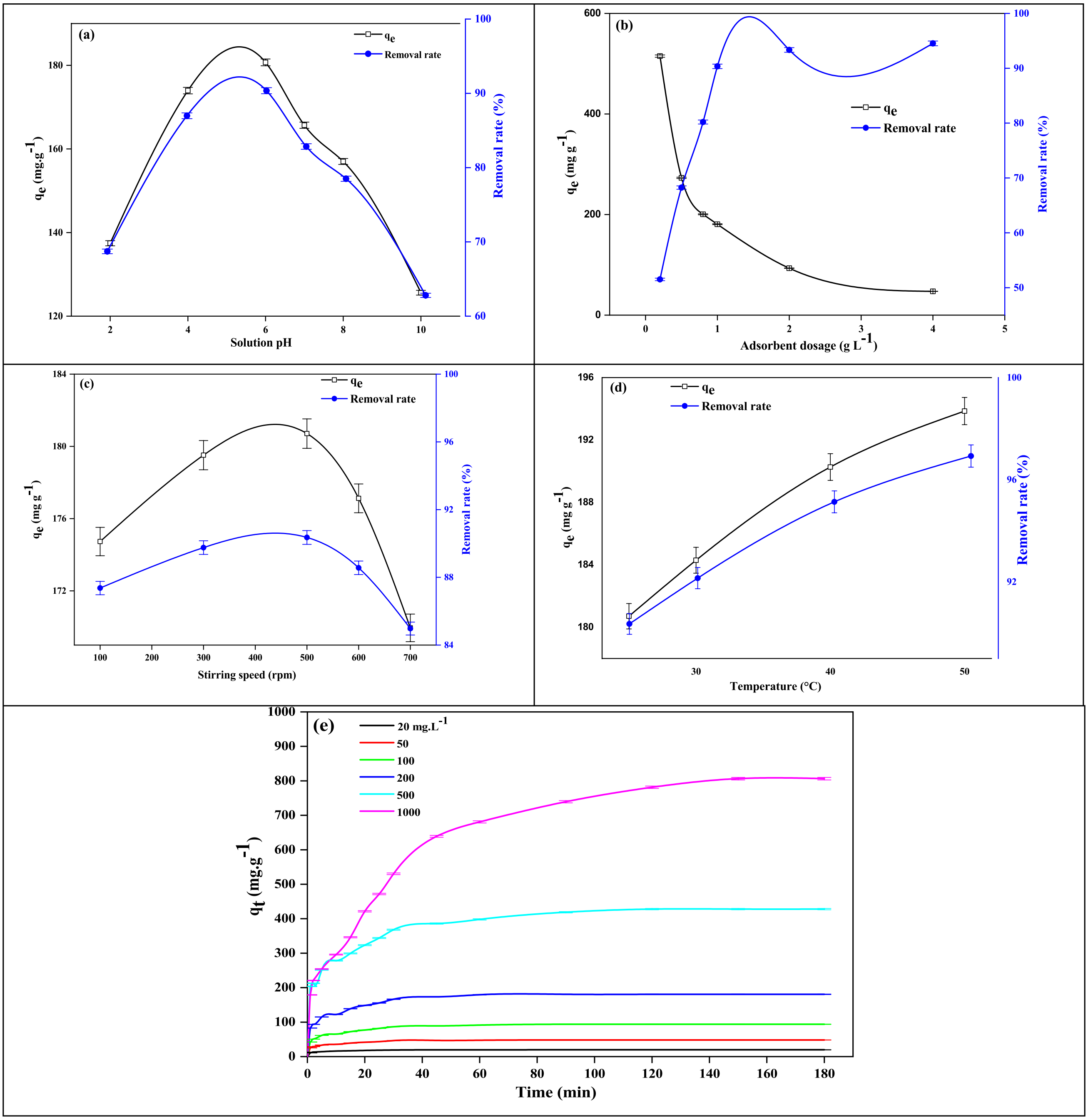

Fig. 8 The influence of different parameters on BR46 adsorption over ACCFP: **a** pH, **b** adsorbent dosages, **c** stirring speed, **d** temperature, and **e** contact time and initial BR46 concentration

and postulates that adsorption heat reduces linearly with coverage (Temkin 1940). The last model was Dubinin-Radushkevich's model (Dubinin 1960). These models may be expressed in the form of the following equations:

$$\mathrm{q_e} = \frac{\mathrm{q_m} \quad \mathrm{K_L} \quad \mathrm{C_e}}{1 + \mathrm{K_L C_e}} \tag{8}$$

$$q_e = K_F \times C_e{}^{1/n} \tag{9}$$

$$q_e = B \ln \left(AC_e\right) \tag{10}$$

$$q_e = q_{DR} e^{-\beta \varepsilon^2} ; \varepsilon = RT\mathrm{Ln}\left(1 + \frac{1}{C_e}\right) \tag{11}$$

Table 4 The study's isotherm models and their associated parameter values

Langmuir	q_m (mg g^{-1})	952.38
	K_L (L mg^{-1})	0.019
	R^2	0.931
Freundlich	K_F	37.021
	$1/n$	0.565
	R^2	0.996
Temkin	A (L mg^{-1})	1.164
	B (J mol^{-1})	108.707
	R^2	0.868
Dubinin-Radushkevich	q_{DR} (mg g^{-1})	207.031
	β	1.578E−7
	R^2	0.715

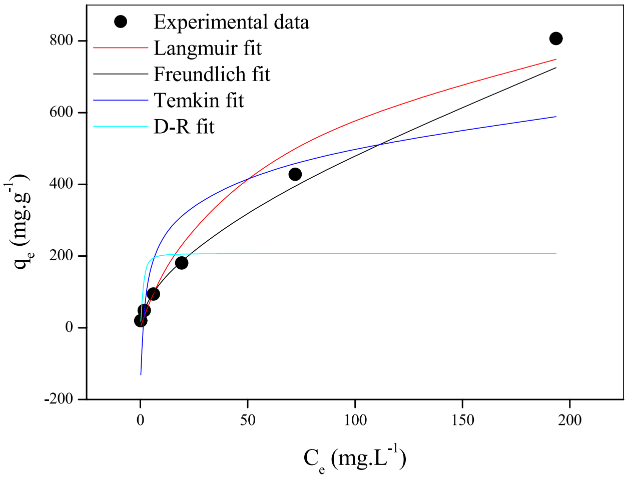

Fig. 9 Adsorption isotherms

q_e, C_e, q_m, and K_L: the equilibrium adsorbed amount (mg g^{-1}) and adsorbate concentration (mg L^{-1}), the monolayer adsorption capacity (mg g^{-1}), and the Langmuir constant (L mg^{-1}).

- K_F and n are the Freundlich constant and adsorption intensity.
- A (L mg^{-1}) and B (J mol^{-1}): constants associated with the most significant binding energy and heat-related adsorption.
- q_{DR} is the monolayer capacity of Dubinin-Radushkevich (mg g^{-1}), β is the sorption energy constant, and ε is the equilibrium concentration (Polanyi potential).

Model adsorption parameters are listed in Table 4 and presented in Fig. 9.

The Freundlich model provides the best match (R^2 = 0.99). However, due to the interactions between the adsorbed molecules, adsorption may occur on a heterogeneous surface due to the isotherm being of type L and the $1/n$ value of 0.56 (Senturk et al. 2010).

Figure 9 illustrates the numerical and experimental findings at 25 °C. According to these observations, the Freundlich model is a good fit for the adsorption of the investigated system. Also, because functional groups are present on the surface of the adsorbent, it is clear that the Freundlich isotherm may be applied to the adsorbent's energy distribution.

Adsorption kinetics

To further understand the reaction mechanism of BR46 adsorption onto ACCFP, we explored the pseudo-first-order (PFO) (Lagergren 1898) and PSO (Ho and McKay 1999) kinetic models. These models' linear representations are given as follows:

$$\ln\left(q_e - q_t\right) = \ln q_e - K_1 t \tag{12}$$

$$\frac{t}{q_t} = \frac{1}{K_2 {q_e}^2} + \frac{1}{q_e} t \tag{13}$$

K_1 (min^{-1}) and K_2 (g mg^{-1} min^{-1}) are the PFO and PSO rate constants. q_e and q_t: BR46 adsorbed quantity (mg g^{-1}) at equilibrium and time (t).

Figure 10a, b show the linear form plots, with the model's parameters in Table 5. The PSO model shows an R^2 value of > 0.99, indicating that this kinetic model describes BR46 adsorption kinetics onto ACCFP. Further evidence that the PSO kinetic model accurately captures the adsorption process is provided by the extraordinarily close agreement between the observed and estimated adsorption capacities using this model (Fig. 10c).

Thermodynamic study

The thermodynamic parameters $\Delta G°$, $\Delta H°$, and $\Delta S°$ denote the spontaneity, heat of sorption, and randomness of the adsorbent-adsorbate interface.

$$\Delta G^{\circ} = -RTlnK_d \tag{14}$$

$$\ln K_d = \frac{\Delta S^{\circ}}{R} - \frac{\Delta H^{\circ}}{RT} \tag{15}$$

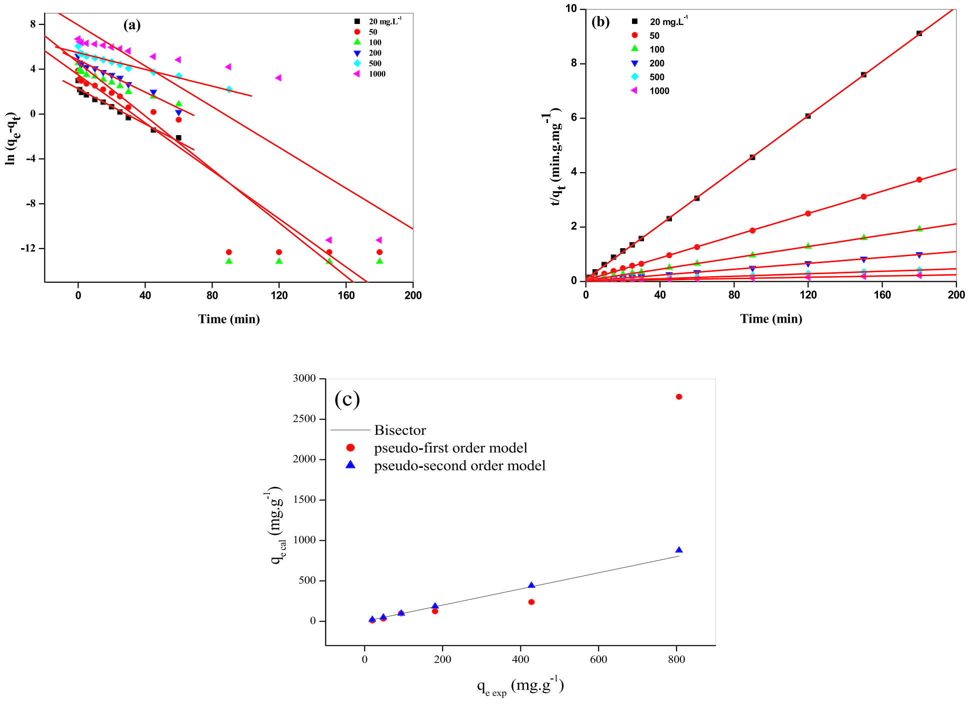

Fig. 10 Adsorption kinetic analysis. Graphical plots of PFO (**a**) and PSO (**b**) and the representation of calculated values according to pseudo-first and pseudo-second order as a function of experimental values (**c**)

Table 5 Kinetic parameters

Concentration	$q_{e\ (exp)}$	PFO			PSO		
		$q_{e\ cal}$	K_1	R^2	$q_{e\ cal}$	K_2	R^2
20	19.743	9.534	0.078	0.982	19.984	0.029	0.999
50	48.122	32.875	0.107	0.942	48.923	0.008	0.999
100	93.854	98.526	0.119	0.935	95.969	0.003	0.999
200	180.707	123.609	0.071	0.985	184.842	0.001	0.999
500	427.865	238.509	0.037	0.979	440.528	4.5E−04	0.999
1000	806.389	2778.093	0.09	0.882	877.193	7.26E−05	0.995

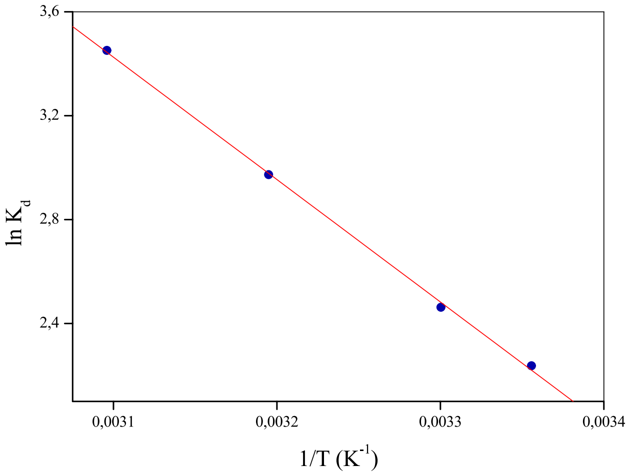

Fig. 11 Plot of Van't Hoff equation

where $K_d = q_e / C_e$. The slope and intercept of Eq. (14) are $\Delta H°$ and $\Delta S°$ (Fig. 11).

As stated in Table 6, all the calculated parameters are supplied. $\Delta G°$ values imply that the adsorption process is spontaneous. These values range from 0 to − 20 kJ mol^{-1}, indicating that physical sorption might regulate the process (Weng and Pan 2007; Deniz and Saygideger 2011).

Table 6 Thermodynamic study results

T (K)	ln K_d	$\Delta G°$ (kJ mol^{-1})	$\Delta H°$ (kJ mol^{-1})	$\Delta S°$ (kJ mol^{-1} K^{-1})
298	4.179	− 5.447	32.512	0.128
303	4.568	− 6.200		
313	5.203	− 7.733		
323	7.294	− 9.263		

Table 7 Descriptors of global reactivity

	E_{HOMO} (eV)	E_{LUMO} (eV)	Gap (eV)	χ	η	ω	ΔN
BR46+	− 8.283	− 6.664	1.619	7.474	0.810	34.498	− 3.182
ACCFP	− 4.425	− 3.905	0.520	4.165	0.260	33.372	-

In contrast, a positive value for ΔH° (32.512 kJ mol^{-1}) implies an endothermic reaction, whereas a positive value for ΔS° (0.128 kJ mol^{-1} K^{-1}) indicates increased randomness at the solid-liquid interface.

Computational study

BR46$^+$ has the most significant HOMO-LUMO gap and hardness, with 1.619 and 0.810 eV values (Table 7). This finding demonstrates that BR46+ is the most stable molecule in this system. Because of its low gap and hardness, ACCFP was the most reactive. The negative calculated ΔN value indicates an electron-accepting ability of the BR46 from the ACCFP.

The developed global electrophilicity index (ω) is the beneficial change in energy when a chemical system approaches saturation through electron addition (Te Velde et al. 2001; Bououden et al. 2021). When electrons move from the HOMO to the LUMO, they lose potency. The HOMO of BR46$^+$ was found on the phenyldiazenyl and phenyl groups' double bonds and the double bound C=N of the triazole moiety (Fig. 12). The LUMO was centered on the azo functional group-bound and its vicinity. Their corresponding energy was − 8.283 eV for the HOMO and − 6.664eV for the LUMO. The HOMO is located on the ACCFP structure's peripheral on the C=C double bonds, while the LUMO is positioned in the center on the C=C bonds. Their equivalent energies are − 4.425 and − 3.905eV.

The charge distribution of the binary interacting system is seen in Fig. 13a. The hydrogen bond acceptor (HBA) is red, the hydrogen bond donor (HBD) is blue, and the nonpolar region is green.

Figure 13b illustrates the BR46$^+$ and ACCFP σ profiles and σ potentials. Surface segments having a screening charge density σ are given a $P(\sigma)$ number (Ma and Ouyang 2013; Chen et al. 2020). There are three types of surfaces: HBD $\sigma \in [-\ 0.025, -\ 0.010]$, nonpolar zone $\sigma \in [-\ 0.010, +\ 0.010]$, and HBA $\sigma \in [+\ 0.010, +\ 0.25]$ (Koyuncu et al. 2018; Xiong et al. 2021).

While examining the potentials of the two molecules with their contact system, it is found that both exhibit an excellent affinity for highly polarized HBAs (Fig. 13b). The ACCFP has a good affinity for HBDs, while the BR46 exhibits no affinity (Cationic molecule). The nonpolar region also noticed a poor affinity between the two molecules. This indicates that physical interactions

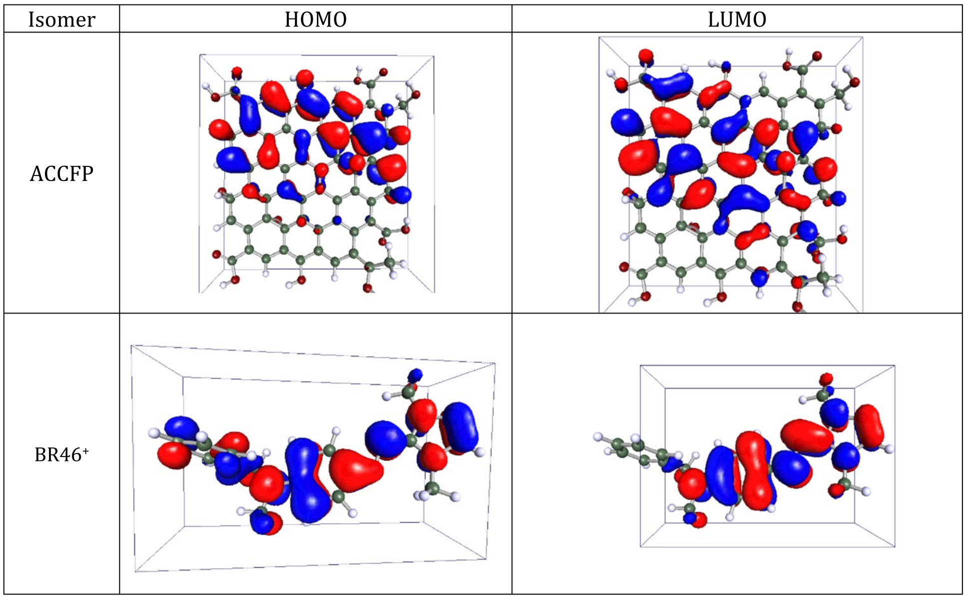

Fig. 12 Frontier molecular orbitals at an iso-surface = 0.02 u.a

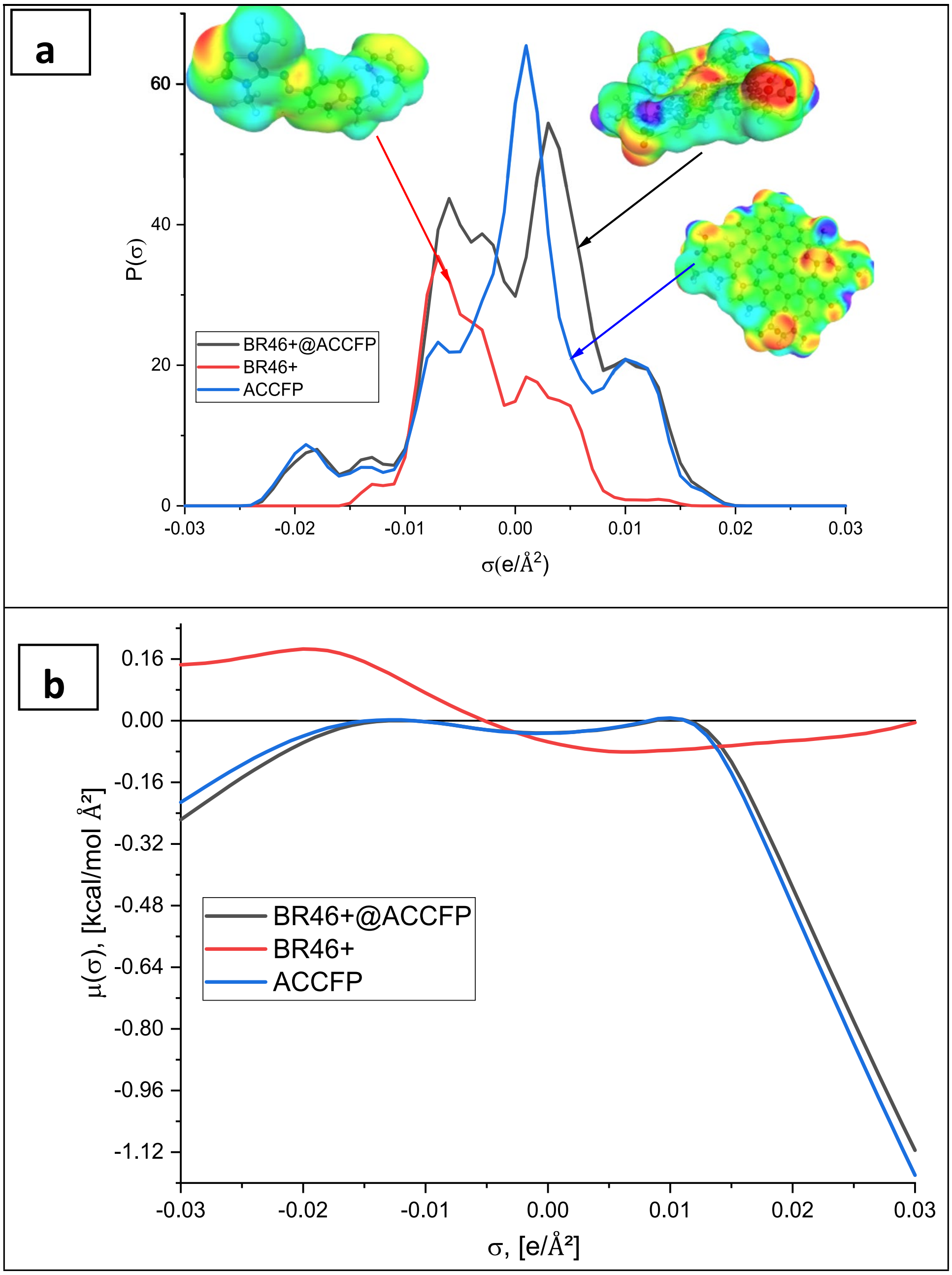

Fig. 13 COSMO-RS study: surfaces, polarities, and potentials

(physical nature) will play a significant role in the interaction between BR46+ and ACCFP, as demonstrated by the AIM research.

Figure 14 shows that the Van der Waals interaction energy contributes the most to mixing the two molecules ($H_{\mathrm{VdW}} = -17.61$ and -33.11 kcal mol^{-1} for BR46$^+$ and ACCFP). Hydrogen bonding (H_{HB}) was found negligible for BR46+ but highly significant as VdW interaction for ACCFP. This shows that the VdW interaction contributes to the adsorption of BR46+ on ACCFP. Electrostatic interaction was less intense but not negligible.

The computed adsorption energy is shown in Table 8. The calculated negative value (− 18.54 eV) indicates the adsorption's attractive and relatively strong nature (Van der Waals forces).

The optimized BR46+@ACCFP complex molecular graph is shown in Fig. 15. Table S3 provides an overview of the topological characteristics of BCP's interactions. The VdW

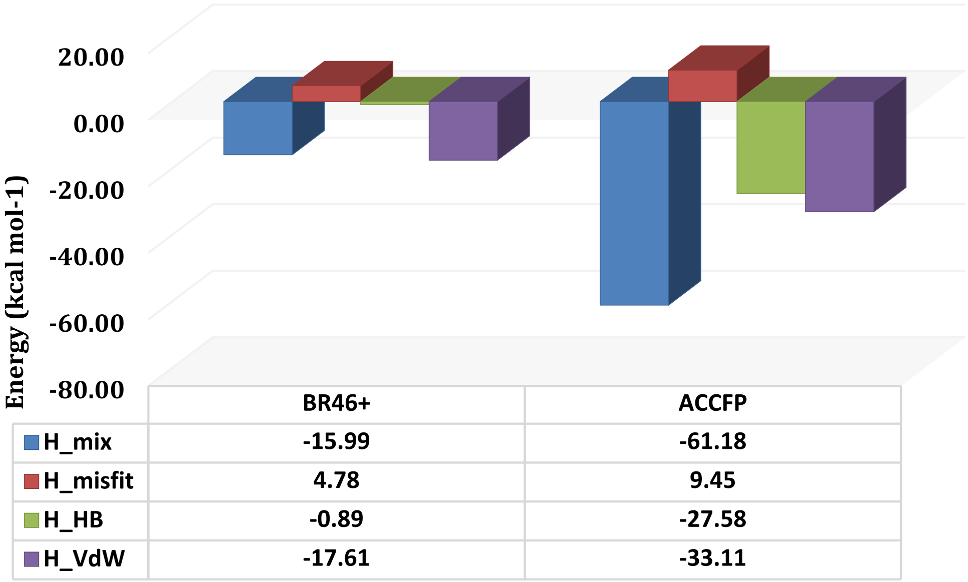

Fig. 14 Interaction energies of the system BR46+@ACCFP

Table 8 Adsorption energies of the complex and free molecules

	BR46+@ ACCFP	BR46+	ACCFP	E_{ads}
Energy (Ha)	− 4537.07	− 1027.18	− 3509.22	− 0.68
Energy (eV)	− 123,460.04	− 27,950.90	− 95,490.60	− 18.54

forces are characterized by relatively low calculated values of $\rho(r)$ in BCPs [3.3×10^{-3}, 9.42×10^{-3}] a.u.

Positive $\nabla^2\rho(r)$ indicates the existence of hydrogen bond (HB) interaction at the 20 BCPs (Table 9). Positive values of $\nabla^2\rho_{BCP}(r)$ and H_{BCP} describe electrostatic interactions (see Fig. 14). $E_{HB} < 0$ implies weak hydrogen bonding strength (Wu et al. 2021b).

Reuse study

The sustainability and durability of the adsorbents are essential factors to consider when developing large-scale applications. Therefore, a stability evaluation must be conducted before deploying ACCFP. This was performed by removing BR46 with 0.1 M (HCl) and regenerating ACCFP for further adsorption cycles. As shown in Fig. 16, following the fourth cycle, adsorption capacity fell from 806.38 to 647.43 mg g^{-1}. The material may be reused four times without substantially compromising its performance. To conduct a comparative analysis of published research on the removal of BR46 using different adsorbents (Table 9). Our analysis indicates that the adsorption capacity is relatively high at 806.36 mg g^{-1},

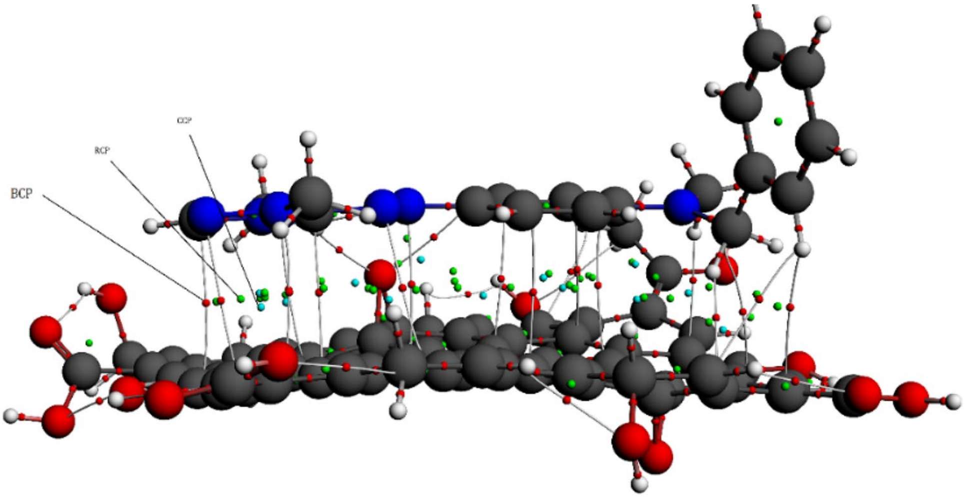

Fig. 15 Molecular graph of the BR46+@ACCFP complex

Table 9 Adsorption of BR6 onto different adsorbents

Adsorbent	Adsorption capacity (mg g^{-1})	Reference
Activated carbon from Ziziphus lotus stones	307	Şentürk and Yıldız (2020)
Wild olive cores activated carbon	781.25	Boudechiche et al., (2019)
Synthesize graphene oxide nano adsorbent	370.4	Shoushtarian et al. (2020)
Activated pine sawdust	312.5	Kaouah et al. (2013)
magnetic nanocomposite Fe@graphite core-shell	46.7	Konicki et al. (2018)
Cactus fruit peels activated carbon	806.38	This study

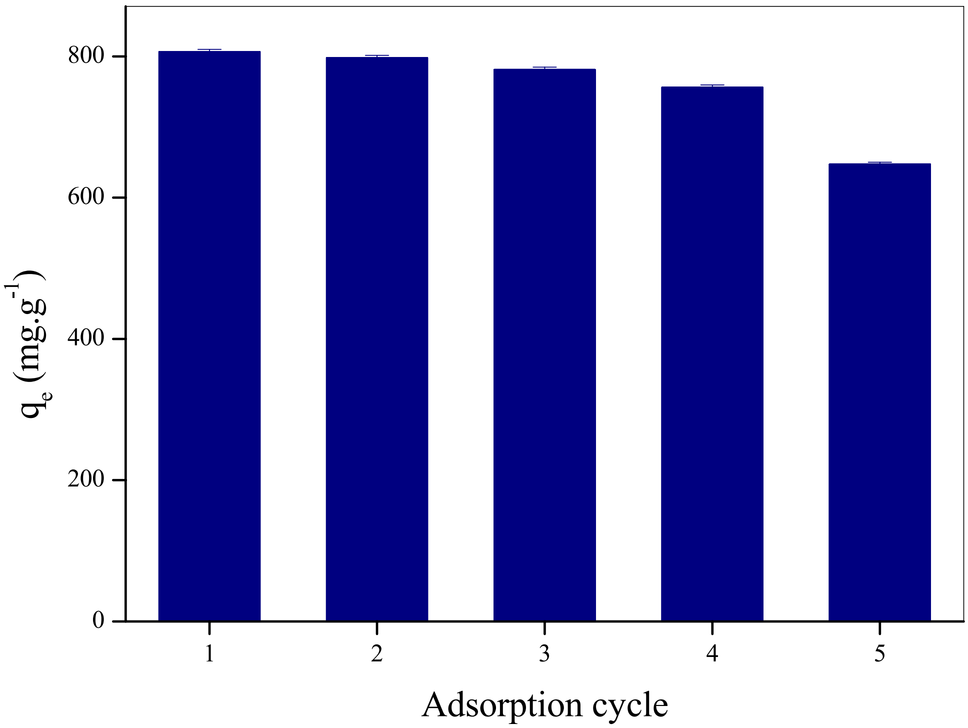

Fig. 16 Reuse and regenerate of ACCFP after successive cycles of adsorption/removal of BR46

which seems to be adequate for treating dye-contaminated wastewater.

Conclusion

By chemical activation with H_3PO_4, activated carbon was produced from cactus fruit peels and physicochemically characterized using XRD, SEM/EDS, XPS, FTIR, BET/BJH, pH_{pzc}, and the Boehm titration. The outcomes reveal the microporosity of the material with a rough heterogeneous surface and a large specific surface area of 1288 m^2 g^{-1} that is well suited for BR46 removal. Adsorption experiments in a batch system were conducted to determine the effect of operational variables such as pH (2–10), adsorbent dosage (0.2–4 g L^{-1}), stirring speed (100–700 rpm), temperature (25–50 °C), time (0–180 min), and initial dye concentration (20–1000 mg L^{-1}), reaching an adsorption capacity of 806.38 mg g^{-1}. The Freundlich model accurately described the adsorption isotherm, despite the pseudo-second-order model expressing the kinetic data with $R^2 \geq 0.995$. Under endothermic circumstances ($\Delta H° = 32.512$ kJ mol^{-1}), the thermodynamic behavior was spontaneous ($\Delta G° < 0$), consistent with an electrostatic contact mechanism. Besides, the stability of ACCFP has been investigated using recyclability testing for up to four consecutive cycles with no discernible loss of effectiveness.

According to the theoretical approach, physical interactions significantly affect the adsorption of BR46+ on ACCFP (physical nature). Overall, the acquired results demonstrated that activated carbon acquired from cactus peels has the potential to be an efficient and eco-friendly adsorbent for treating colored wastewaters.

Supplementary Information The online version contains supplementary material available at https://doi.org/10.1007/s11356-022-22402-4.

Data availability Not applicable.

Author contribution Imane Akkari, Zahra Graba, Nacer Bezzi, Mohamed Mehdi Kaci, Farid Ait Merzeg, Nadia Bait, and Azedine Ferhati: conceptualization, interpretation of results, and writing and editing. Guilherme L. Dotto and Yacine Benguerba: theoretical study, interpretation of results, and writing and editing.

Funding The study was financially supported by the Algerian Ministry of Higher Education and the University of Bejaia.

Declarations

Ethical approval Not applicable.

Consent to participate Not applicable.

Consent for publication Not applicable.

Conflict of interest The authors declare no competing interests.

References

Abatan OG, Oni BA, Agboola O et al (2019) Production of activated carbon from African star apple seed husks, oil seed and whole seed for wastewater treatment. Journal of Cleaner Production 232:441–450. https://doi.org/10.1016/j.jclepro.2019.05.378

Aissaoui T, Benguerba Y, AlNashef IM (2017) Theoretical investigation on the microstructure of triethylene glycol based deep eutectic solvents: COSMO-RS and TURBOMOLE prediction. Journal of Molecular Structure 1141:451–456

Akkari I, Graba Z, Bezzi N, et al (2022) Biosorption of Basic Red 46 using raw cactus fruit peels: equilibrium, kinetic and thermodynamic studies. Biomass Conversion and Biorefinery 1–12

Almustafa G, Darwish AS, Lemaoui T et al (2021) Liquification of 2, 2, 4-trimethyl-1, 3-pentanediol into hydrophobic eutectic mixtures: a multi-criteria design for eco-efficient boron recovery. Chemical Engineering Journal 426:131342

Arora C, Soni S, Sahu S et al (2019) Iron based metal organic framework for efficient removal of methylene blue dye from industrial waste. Journal of Molecular Liquids 284:343–352. https://doi.org/10.1016/j.molliq.2019.04.012

Atmani F, Kaci MM, Yeddou-Mezenner N et al (2022) Insights into the physicochemical properties of suger scum as a sustainable biosorbent derived from sugar refinery waste for efficient cationic dye removal. Biomass Conversion and Biorefinery 1-15. https://doi.org/10.1007/s13399-022-02646-3

Bagheri A, Abu-Danso E, Iqbal J, Bhatnagar A (2020) Modified biochar from Moringa seed powder for the removal of diclofenac from aqueous solution. Environmental Science and Pollution Research 27:7318–7327

Baysal M, Bilge K, Yılmaz B et al (2018) Preparation of high surface area activated carbon from waste-biomass of sunflower piths: kinetics and equilibrium studies on the dye removal. Journal of Environmental Chemical Engineering 6:1702–1713. https://doi.org/10.1016/j.jece.2018.02.020

Benabid S, Benguerba Y, AlNashef IM, Haddaoui N (2019a) Theoretical study of physicochemical properties of selected ammonium salt-based deep eutectic solvents. Journal of Molecular Liquids 285:38–46. https://doi.org/10.1016/j.molliq.2019.04.052

Benabid S, Haddaoui N, Lemaoui T et al (2021) Computational modeling of polydecanediol-co-citrate using benzalkonium chloride-based hydrophobic eutectic solvents: COSMO-RS, reactivity, and compatibility insights. Journal of Molecular Liquids 339:116674

Benabid S, Streit AFM, Benguerba Y et al (2019b) Molecular modeling of anionic and cationic dyes adsorption on sludge derived activated carbon. Journal of Molecular Liquids 289:111119. https://doi.org/10.1016/j.molliq.2019.111119

Berraaouan A, Abderrahim Z, Hassane M et al (2015) Evaluation of protective effect of cactus pear seed oil (Opuntia ficus-indica L. MILL.) against alloxan-induced diabetes in mice. Asian Pacific Journal of Tropical Medicine 8:532–537

Boehm H (2002) Surface oxides on carbon and their analysis: a critical assessment. Carbon 40:145–149. https://doi.org/10.1016/S0008-6223(01)00165-8

Boudechiche N, Fares M, Ouyahia S et al (2019) Comparative study on removal of two basic dyes in aqueous medium by adsorption using activated carbon from Ziziphus lotus stones. Microchemical Journal 146:1010–1018. https://doi.org/10.1016/j.microc.2019.02.010

Bououden W, Benguerba Y, Darwish AS et al (2021) Surface adsorption of crizotinib on carbon and boron nitride nanotubes as anti-cancer drug carriers: COSMO-RS and DFT molecular insights. Journal of Molecular Liquids 338:116666. https://doi.org/10.1016/j.molliq.2021.116666

Chen L, Süß D, Sukuba I et al (2020) Performance of DFT functionals for properties of small molecules containing beryllium, tungsten and hydrogen. Nuclear Materials and Energy 22:100731. https://doi.org/10.1016/j.nme.2020.100731

Darwish AS, Warrag SEE, Lemaoui T et al (2021) Green extraction of volatile fatty acids from fermented wastewater using hydrophobic deep eutectic solvents. Fermentation 7:226

Deniz F, Saygideger SD (2011) Removal of a hazardous azo dye (Basic Red 46) from aqueous solution by princess tree leaf. Desalination 268:6–11. https://doi.org/10.1016/j.desal.2010.09.043

Dubinin M (1960) The potential theory of adsorption of gases and vapors for adsorbents with energetically nonuniform surfaces. Chemical reviews 60(2):235–241. https://doi.org/10.1021/cr60204a006

Elmouwahidi A, Castelo-Quibén J, Vivo-Vilches JF et al (2018) Activated carbons from agricultural waste solvothermally doped with sulphur as electrodes for supercapacitors. Chemical Engineering Journal 334:1835–1841. https://doi.org/10.1016/j.cej.2017.11.141

Enniya I, Rghioui L, Jourani A (2018) Adsorption of hexavalent chromium in aqueous solution on activated carbon prepared from apple peels. Sustainable Chemistry and Pharmacy 7:9–16. https://doi.org/10.1016/j.scp.2017.11.003

Francoeur M, Ferino-Pérez A, Yacou C et al (2021) Activated carbon synthetized from Sargassum (sp) for adsorption of caffeine: understanding the adsorption mechanism using molecular modeling. Journal of Environmental Chemical Engineering 9:104795

Freundlich HMF (1906) Over the adsorption in solution. J Phys chem 57 (3854

Gebrezgiher M, Kiflie Z (2020) Utilization of cactus peel as biosorbent for the removal of reactive dyes from textile dye effluents. J Environ Public Health 2020

Goswami M, Phukan P (2017) Enhanced adsorption of cationic dyes using sulfonic acid modified activated carbon. Journal of

Environmental Chemical Engineering 5:3508–3517. https://doi.org/10.1016/j.jece.2017.07.016

Grabowski SJ, Ugalde JM (2010) Bond paths show preferable interactions: ab initio and QTAIM studies on the X– H··· π hydrogen bond. The Journal of Physical Chemistry A 114:7223–7229

Hameed BH, Ahmad AA (2009) Batch adsorption of methylene blue from aqueous solution by garlic peel, an agricultural waste biomass. Journal of Hazardous Materials 164:870–875. https://doi.org/10.1016/j.jhazmat.2008.08.084

Hammoudi N-E-H, Benguerba Y, Attoui A et al (2022) In silico drug discovery of IKK-β inhibitors from 2-amino-3-cyano-4-alkyl-6-(2-hydroxyphenyl) pyridine derivatives based on QSAR, docking, molecular dynamics and drug-likeness evaluation studies. Journal of Biomolecular Structure and Dynamics 40:886–902

Hammoudi NE, Sobhi W, Attoui A, Lemaoui T et al (2021) In silico drug discovery of acetylcholinesterase and butyrylcholinesterase enzymes inhibitors based on quantitative structure-activity relationship (QSAR) and drug-likeness evaluation. Journal of Molecular Structure 1229:129845

Ho Y, McKay G (1999) Pseudo-second order model for sorption processes. Process Biochemistry 34:451–465. https://doi.org/10.1016/S0032-9592(98)00112-5

Jang E, Choi SW, Hong S-M et al (2018) Development of a cost-effective CO2 adsorbent from petroleum coke via KOH activation. Applied Surface Science 429:62–71

Jawad AH, Mohd Firdaus Hum NN, Abdulhameed AS, Mohd Ishak MA (2020) Mesoporous activated carbon from grass waste via H3PO4-activation for methylene blue dye removal: modelling, optimisation, and mechanism study. Intl J Environ Anal Chem 1–17

Jawad AH, Saud Abdulhameed A, Wilson LD et al (2021) High surface area and mesoporous activated carbon from KOH-activated dragon fruit peels for methylene blue dye adsorption: optimization and mechanism study. Chinese Journal of Chemical Engineering 32:281–290. https://doi.org/10.1016/j.cjche.2020.09.070

Kaci MM, Nasrallah N, Atmani F et al (2021a) Enhanced photocatalytic performance of CuAl2O4 nanoparticles spinel for dye degradation under visible light. Research on Chemical Intermediates 47:3785–3806

Kaci MM, Nasrallah N, Djaballah AM et al (2022) Insights into the optical and electrochemical features of CuAl2O4 nanoparticles and it use for methyl violet oxidation under sunlight exposure. Optical Materials 126:112198. https://doi.org/10.1016/j.optmat.2022.112198

Kaci MM, Nasrallah N, Kebir M et al (2021b) Synthesis, physical and electrochemical properties of CoMn2O4: application to photocatalytic Ni2+ reduction. Research on Chemical Intermediates 47:1693–1712

Kaouah F, Boumaza S, Berrama T et al (2013) Preparation and characterization of activated carbon from wild olive cores (oleaster) by H3PO4 for the removal of Basic Red 46. Journal of Cleaner Production 54:296–306

Konicki W, Hełminiak A, Arabczyk W, Mijowska E (2018) Adsorption of cationic dyes onto Fe@graphite core–shell magnetic nanocomposite: equilibrium, kinetics and thermodynamics. Chemical Engineering Research and Design 129:259–270. https://doi.org/10.1016/j.cherd.2017.11.004

Koyuncu F, Güzel F, Sayğılı H (2018) Role of optimization parameters in the production of nanoporous carbon from mandarin shells by microwave-assisted chemical activation and utilization as dye adsorbent. Advanced Powder Technology 29:2108–2118

Kumar A, Jena HM (2017) Adsorption of Cr(VI) from aqueous solution by prepared high surface area activated carbon from Fox nutshell by chemical activation with H3PO4. Journal of Environmental Chemical Engineering 5:2032–2041. https://doi.org/10.1016/j.jece.2017.03.035

Kumar R, Barakat MA (2013) Decolourization of hazardous brilliant green from aqueous solution using binary oxidized cactus fruit peel. Chemical engineering journal 226:377–383

Kuppusamy S, Venkateswarlu K, Thavamani P et al (2017) Quercus robur acorn peel as a novel coagulating adsorbent for cationic dye removal from aquatic ecosystems. Ecological Engineering 101:3–8. https://doi.org/10.1016/j.ecoleng.2017.01.014

Kurnia KA, Lima F, Cláudio AFM et al (2015) Hydrogen-bond acidity of ionic liquids: an extended scale. Physical Chemistry Chemical Physics 17:18980–18990

Lagergren SK (1898) About the theory of so-called adsorption of soluble substances. Sven Vetenskapsakad Handingarl 24:1–39

Langmuir I (1918) The adsorption of gases on plane surfaces of glass, mica and platinum. Journal of the American chemical society 40:1361–1403

Lemaoui T, Abu Hatab F, Darwish AS et al (2021) Molecular-based guide to predict the pH of eutectic solvents: promoting an efficient design approach for new green solvents. ACS Sustainable Chemistry and Engineering 9:5783–5808. https://doi.org/10.1021/acssuschemeng.0c07367

Lemaoui T, Darwish AS, Attoui A et al (2020a) Predicting the density and viscosity of hydrophobic eutectic solvents: towards the development of sustainable solvents. Green Chemistry 22:8511–8530. https://doi.org/10.1039/D0GC03077E

Lemaoui T, Darwish AS, Hammoudi NEH et al (2020b) Prediction of electrical conductivity of deep eutectic solvents using COSMO-RS sigma profiles as molecular descriptors: a quantitative structure-property relationship study. Industrial and Engineering Chemistry Research 59:13343–13354. https://doi.org/10.1021/acs.iecr.0c02542

Lemaoui T, Hammoudi NEH, Alnashef IM et al (2020c) Quantitative structure properties relationship for deep eutectic solvents using Sσ-profile as molecular descriptors. Journal of Molecular Liquids 309:113165

Lemaoui T, Hammoudi NEH, Benguerba Y, Attoui A (2020d) Molecular docking of new active compounds towards the acetylcholinesterase enzyme. Current Research in Bioinformatics 8:18–20

Liu Q-S, Zheng T, Wang P, Guo L (2010) Preparation and characterization of activated carbon from bamboo by microwave-induced phosphoric acid activation. Industrial Crops and Products 31:233–238. https://doi.org/10.1016/j.indcrop.2009.67011

Ma X, Ouyang F (2013) Adsorption properties of biomass-based activated carbon prepared with spent coffee grounds and pomelo skin by phosphoric acid activation. Applied Surface Science 268:566–570

Mateo W, Lei H, Villota E et al (2020) Synthesis and characterization of sulfonated activated carbon as a catalyst for bio-jet fuel production from biomass and waste plastics. Bioresource technology 297:122411

Mohamed SK, Alazhary AM, Al-Zaqri N et al (2020) Cost-effective adsorbent from arabinogalactan and pectin of cactus pear peels: kinetics and thermodynamics studies. International Journal of Biological Macromolecules 150:941–947

Mohanty K, Jha M, Meikap BC, Biswas MN (2005) Removal of chromium (VI) from dilute aqueous solutions by activated carbon developed from Terminalia arjuna nuts activated with zinc chloride. Chemical Engineering Science 60:3049–3059. https://doi.org/10.1016/j.ces.2004.12.049

Mokhtar N, Aziz EA, Aris A et al (2017) Biosorption of azo-dye using marine macro-alga of Euchema Spinosum. Journal of Environmental Chemical Engineering 5:5721–5731. https://doi.org/10.1016/j.jece.2017.10.043

Momčilović MZ, Onjia AE, Purenović MM et al (2012) Removal of cationic dye from water by activated pine cones. Journal of the Serbian Chemical Society 77:761–774

Mukherjee T, Ghosh SK, Rahaman M (2019) Determining the quality of activated carbon using L16 Taguchi method through waste tyre recycling. In: Waste Water Recycling and Management. Springer, pp 27–36

Naushad M, Alqadami AA, AlOthman ZA et al (2019) Adsorption kinetics, isotherm and reusability studies for the removal of cationic dye from aqueous medium using arginine modified activated carbon. Journal of Molecular Liquids 293:111442. https://doi.org/10.1016/j.molliq.2019.111442

Niazi L, Lashanizadegan A, Sharififard H (2018) Chestnut oak shells activated carbon: Preparation, characterization and application for Cr (VI) removal from dilute aqueous solutions. Journal of cleaner production 185:554–561

Novais RM, Caetano APF, Seabra MP et al (2018) Extremely fast and efficient methylene blue adsorption using eco-friendly cork and paper waste-based activated carbon adsorbents. Journal of Cleaner Production 197:1137–1147. https://doi.org/10.1016/j.jclepro.2018.06.278

Paz A, Carballo J, Pérez MJ, Domínguez JM (2017) Biological treatment of model dyes and textile wastewaters. Chemosphere 181:168–177

Prastuti OP, Septiani EL, Kurniati Y, Setyawan H (2019) Banana peel activated carbon in removal of dyes and metals ion in textile industrial waste. In: Materials Science Forum. Trans Tech Publ:204–209

Rengaraj S, Kim Y, Joo CK et al (2004) Batch adsorptive removal of copper ions in aqueous solutions by ion exchange resins: 1200H and IRN97H. Korean Journal of Chemical Engineering 21:187–194. https://doi.org/10.1007/BF02705397

Rozas I, Alkorta I, Elguero J (2000) Behavior of ylides containing N, O, and C atoms as hydrogen bond acceptors. Journal of the American Chemical Society 122:11154–11161

Ruiz B, Ferrera-Lorenzo N, Fuente E (2017) Valorisation of lignocellulosic wastes from the candied chestnut industry. Sustainable activated carbons for environmental applications. Journal of Environmental Chemical Engineering 5:1504–1515

Saenz C (2000) Processing technologies: an alternative for cactus pear (Opuntia spp.) fruits and cladodes. Journal of Arid Environments 46:209–225. https://doi.org/10.1006/jare.2000.0676

Senturk HB, Ozdes D, Duran C (2010) Biosorption of Rhodamine 6G from aqueous solutions onto almond shell (Prunus dulcis) as a low cost biosorbent. Desalination 252:81–87. https://doi.org/10.1016/j.desal.2009.10.021

Şentürk İ, Yıldız MR (2020) Highly efficient removal from aqueous solution by adsorption of Maxilon Red GRL dye using activated pine sawdust. Korean Journal of Chemical Engineering 37:985–999

Shainyan BA, Chipanina NN, Aksamentova TN et al (2010) Intramolecular hydrogen bonds in the sulfonamide derivatives of oxamide, dithiooxamide, and biuret. FT-IR and DFT study. AIM and NBO analysis. Tetrahedron 66:8551–8556. https://doi.org/10.1016/j.tet.2010.08.076

Shetty AA, Rana MK, Preetham SP (2012) Cactus: a medicinal food. Journal of food science and technology 49:530–536

Shoushtarian F, Moghaddam MRA, Kowsari E (2020) Efficient regeneration/reuse of graphene oxide as a nanoadsorbent for removing basic Red 46 from aqueous solutions. Journal of Molecular Liquids 312:113386. https://doi.org/10.1016/j.molliq.2020.113386

Souza PR, Dotto GL, Salau NPG (2018) Artificial neural network (ANN) and adaptive neuro-fuzzy interference system (ANFIS) modelling for nickel adsorption onto agro-wastes and commercial activated carbon. Journal of Environmental Chemical Engineering 6:7152–7160. https://doi.org/10.1016/j.jece.2018.11.013

Tang SH, Ahmad Zaini MA (2020) Development of activated carbon pellets using a facile low-cost binder for effective malachite green dye removal. Journal of Cleaner Production 253:119970. https://doi.org/10.1016/j.jclepro.2020.119970

Te Velde GT, Bickelhaupt FM, Baerends EJ et al (2001) Chemistry with ADF. Journal of Computational Chemistry 22:931–967

Temkin MI (1940) Kinetics of ammonia synthesis on promoted iron catalysts. Actaphysiochim URSS 12:327–335

Toumi K-H, Benguerba Y, Erto A et al (2019) Efficient removal of cationic dyes from aqueous solutions using the low-cost algerian olive cake waste adsorbent. Jom 71:791–800

Vieira WT, Bispo MD, de Melo FS et al (2021) Activated carbon from macauba endocarp (Acrocomia aculeate) for removal of atrazine: experimental and theoretical investigation using descriptors based on DFT. Journal of Environmental Chemical Engineering 9:105155. https://doi.org/10.1016/j.jece.2021.105155

Weng C-H, Pan Y-F (2007) Adsorption of a cationic dye (methylene blue) onto spent activated clay. Journal of Hazardous Materials 144:355–362. https://doi.org/10.1016/j.jhazmat.2006.09.097

Wong S, Yac'cob NAN, Ngadi N et al (2018) From pollutant to solution of wastewater pollution: Synthesis of activated carbon from textile sludge for dye adsorption. Chinese Journal of Chemical Engineering 26:870–878. https://doi.org/10.1016/j.cjche.2017.07.015

Wu J, Wang J, Guan T et al (2021a) Adsorption and decolorization of hydrogenated coal tar on resin-based activated carbon spheres. Carbon 183:1014–1015. https://doi.org/10.1016/j.carbon.2021.07.096

Wu S, Yan P, Yang W et al (2021b) ZnCl2 enabled synthesis of activated carbons from ion-exchange resin for efficient removal of Cu2+ ions from water via capacitive deionization. Chemosphere 264:128557

Xiao W, Garba ZN, Sun S et al (2020) Preparation and evaluation of an effective activated carbon from white sugar for the adsorption of rhodamine B dye. Journal of Cleaner Production 253:119989. https://doi.org/10.1016/j.jclepro.2020.119989

Xiong H, Xiao Y, Yan Z (2021) Preparation of activated carbon and its adsorption of naphthalene in liquid paraffin oil. Colloid and Interface Science Communications 43:100460. https://doi.org/10.1016/j.colcom.2021.100460

Xue H, Wang X, Xu Q et al (2022) Adsorption of methylene blue from aqueous solution on activated carbons and composite prepared from an agricultural waste biomass: a comparative study by experimental and advanced modeling analysis. Chemical Engineering Journal 430:132801

Yu L, Luo Y (2014) The adsorption mechanism of anionic and cationic dyes by Jerusalem artichoke stalk-based mesoporous activated carbon. Journal of Environmental Chemical Engineering 2:220–229. https://doi.org/10.1016/j.jece.2013.12.016

Zhao D, Zhang W, Chen C, Wang X (2013) Adsorption of methyl orange dye onto multiwalled carbon nanotubes. Procedia Environmental Sciences 18:890–895. https://doi.org/10.1016/j.proenv.2013.04.120